Latypova, Renata; Seppala, Oskari; Nyo, Tun Tun; Kauppi, Timo; Pallaspuro, Sakari; Mehtonen, Saara; Hanninen, Hannu; Kömi, Jukka

Hydrogen-Induced Cracking of 500 HBW Steels Studied Using a Novel Tuning-Fork Test with Integrated Loadcell System

Published in:
Corrosion

DOI:
10.5006/3592

Published: 20/07/2020

Document Version
Peer-reviewed accepted author manuscript, also known as Final accepted manuscript or Post-print

Please cite the original version:
Latypova, R., Seppala, O., Nyo, T. T., Kauppi, T., Pallaspuro, S., Mehtonen, S., Hanninen, H., & Kömi, J. (2020). Hydrogen-Induced Cracking of 500 HBW Steels Studied Using a Novel Tuning-Fork Test with Integrated Loadcell System. *Corrosion*, *76*(10), 917-966. https://doi.org/10.5006/3592

Hydrogen-induced cracking of 500 HBW steels studied using a novel tuning-fork test with integrated loadcell system

Renata Latypova, ‡,* Oskari Seppälä,* Tun Tun Nyo,* Timo Kauppi,*,** Sakari Pallaspuro,* Saara Mehtonen, *** Hannu Hänninen,**** and Jukka Kömi*

‡Corresponding author. E-mail: renata.latypova@oulu.fi

* Materials and Mechanical Engineering, Centre for Advanced Steels Research (CASR), University of Oulu, P.O. Box 4200, 90014 Oulu, Finland

** Arctic Steel and Mining RDI-group, Lapland University of Applied Science, 94600 Kemi, Finland

*** SSAB, P.O. Box 93, 92101 Raahe, Finland

**** Aalto University School of Engineering, Department of Mechanical Engineering, P.O. Box 14200, FI-00076 AALTO, Finland

ABSTRACT

Hydrogen embrittlement is a well-known problem with high-strength steels. An important aspect of hydrogen embrittlement research is the effect of the prior austenite grain (PAG) structure on hydrogen-induced fracture. The microstructural anisotropy of PAG structure depends on the steel manufacturing process. In this study, 500 HBW martensitic steels with different PAG structures are investigated with a novel tuning-fork test that utilizes an integrated loadcell system. The loadcell clamping system is used during hydrogen charging allowing tracking of the applied force throughout the tests, which enables detection of separate phases of cracking and time-to-fracture. The elongated PAG morphology produces different results depending on the crack path direction in relation to the rolling direction, whereas the equiaxed PAG morphology does not manifest an orientation dependence. Depending on the PAG shape, also the fracture morphology differs. Time-to-fracture results show that elongated grain morphologies with transgranular quasi-cleavage crack propagation are more beneficial against hydrogen-induced fracture than equiaxed grain structure with intergranular crack propagation. Our results demonstrate that the shape of the PAG structure plays an important role in the crack propagation mechanism and that it is important to consider the possible direction of hydrogen-induced cracks in the final structural applications.

KEY WORDS: *grain morphology, hydrogen embrittlement, martensite, steel*

1 INTRODUCTION

There is an increasing demand for high-strength steels due to economical necessities and environmental impacts [1]. Higher strength provides possibilities to use lighter steel structures, which correspond to energy efficiency, cost savings, and reduced carbon footprint [2]. However, the use of high-strength steels may be restricted, e.g. due to susceptibility to hydrogen-induced failure, such as hydrogen embrittlement (HE) and hydrogen-induced stress corrosion cracking (HISCC) [3,4]. Overall, HE susceptibility depends on several factors such as the microstructure, environment, and stress level and state. The final microstructure of a steel, which depends on the alloy composition as well as its processing, affects markedly hydrogen diffusion and trapping properties. [1]

Depending on the microstructure, there are different number and types of hydrogen traps such as dislocations, grain boundaries, precipitates, and inclusions. These traps can increase or decrease the HE susceptibility since hydrogen traps affect hydrogen solubility and diffusivity. For example, the interaction of impurities (S, P, Sb) with hydrogen can embrittle prior austenite grain boundaries (PAGs) and cause intergranular fracture. In the case of sulfur, embrittlement is connected to the formation of MnS inclusion stringers [3]. Too high number of MnS inclusions and segregation bands can also affect centerline segregation, which has detrimental effects on hydrogen-induced cracking resistance of steels [5].

Martensitic high-strength steels may be produced in several ways [3]. The traditional process utilizes reheating and quenching (RQ) with possible tempering (QT). Austenite is traditionally recrystallized before quenching, which produces an equiaxed PAG structure. As an alternative to the conventional processes, martensitic high-strength steels can be produced via combined thermomechanical processing and direct-quenching (DQ), which produces elongated/pancaked PAGs parallel to the rolling direction [6]. The PAGs are elongated due to the rolling below the recrystallization stop temperature before quenching. A similar elongated PAG structure can be achieved also by ausforming [7] or tempforming [8] treatments, which utilize deformation at even lower temperatures compared to the DQ process. Elongated PAG structure creates a microstructural anisotropy, which is known to affect for example the formability of steels [6].

In this study, the investigated steel grades are abrasion-resistant martensitic steels, which are used in transportation as well as in processing and mining industries. Due to their high strength, abrasion-resistant steels are susceptible to hydrogen-induced failures. For example, in the mining industry, mineral contents in the mine water can cause HISCC[9]. There are many testing methods for studying HE and SCC of high-strength steels, where notched/smooth specimens are investigated under applied mechanical load in a hydrogen charging environment. The most commonly utilized current testing methods are: constant load tests [10,11], constant displacement tests with e.g. C-ring [12,13] and U-bend specimens [14,15], slow strain rate tests (SSRT) or constant extension rate tests (CERT) [16] and linearly increasing stress tests (LIST) [17]. From these testing methods, constant displacement tests are the most straightforward and inexpensive to perform, but they have some disadvantages [18]. In constant displacement tests, specimens are loaded to a fixed displacement and then exposed to a selected environment [19]. The pre-loading prior to the immersion to a hydrogen-containing environment can lead to non-conservative results and a high degree of scatter in the data [18,19]. Constant-displacement tests may also require an arbitrarily chosen testing time for the determination of threshold stress (σ_{th}) or time-to-fracture (t_f) [18].

A novel constant-displacement testing method for evaluating the HE susceptibility of martensitic high-strength steels has been developed [20,21]. Initially, tuning-fork tests (TFT) were conducted under galvanostatic [20] or potentiostatic [21] hydrogen charging conditions and used for ranking of high-strength steels by the determination of σ_{th}. The testing method is here developed further by adding a loadcell clamping system, which improves loading accuracy and eliminates unpredictable testing time issues with relatively short testing times. In comparison to the other available testing methods, TFT has several advantages. The main advantage is the specimen geometry with a superior stress control, which is achieved without a tensile test equipment. TFT has proven to be a rapid test that can provide data regarding the crack initiation, propagation, and final time-to-fracture in a matter of hours. Variability of the data is small, and the tests have good repeatability. In addition to time-to-fracture, trustworthy threshold stress level can be determined with a longer testing period [21] by applying the binary search procedure according to SFS-EN ISO 7539-1 [22]. The results can be utilized to study and rank the hydrogen-induced fracture resistance of high-strength steels. In this study, TFT was utilized to obtain a deeper understanding about the effect of the different PAG morphologies on hydrogen-induced failure.

2 EXPERIMENTAL PROCEDURES

2.1 Test materials

Three hot-rolled, medium-carbon steel grades with a martensitic microstructure and a nominal hardness of 500 HBW are studied. Two of the steel grades were manufactured by a direct-quenching (DQ) process, and one by the conventional reheating and quenching process (RQ). Tensile tests of the materials were conducted with specimens oriented longitudinal (L) and transverse (T) to the rolling direction. Table 1 summarizes the mechanical properties and relevant chemical composition of each steel grade.

TABLE 1. Mechanical properties and carbon, manganese and sulfur contents of the test materials (in wt.%).

Steel grade	C	Mn	S	Measured hardness (HBW)	0.2 % offset yield stress = YS (MPa)	Tensile strength = TS (MPa)	YS/TS
DQ_1 L	0.25	0.25	0.002	487	1411	1632	0.86
DQ_1 T					1384	1629	0.85
DQ_2 L	0.26	1.14	0.003	495	1404	1582	0.89
DQ_2 T					1417	1642	0.86
RQ L	0.24	0.68	0.001	514	1465	1654	0.89
RQ T					1426	1653	0.86

Manufacturing process affect the PAG structure of the tested steel grades. The DQ process results in an elongated/pancaked and RQ in equiaxed PAG morphology (Figure 1). The average grain size, grain boundary surface area per unit volume S_v, and RD/ND index of each steel grade are given in Table 2. Mean PAG sizes were calculated with a novel grain size calculator program [23,24] to obtain a better statistical accuracy. The program utilizes the mean lineal intercept method, and grain sizes were calculated for all three RD-ND, RD-TD and TD-ND sections. The degree of elongation was the highest for DQ_1 with a RD/ND size ratio of 3. DQ_2 had a more moderate degree of elongation with a RD/ND ratio of 2, but it had also a bigger grain size compared to the DQ_1 and RQ. For RQ, the PAG morphology was equiaxed and the average grain size was the same as for DQ_1.

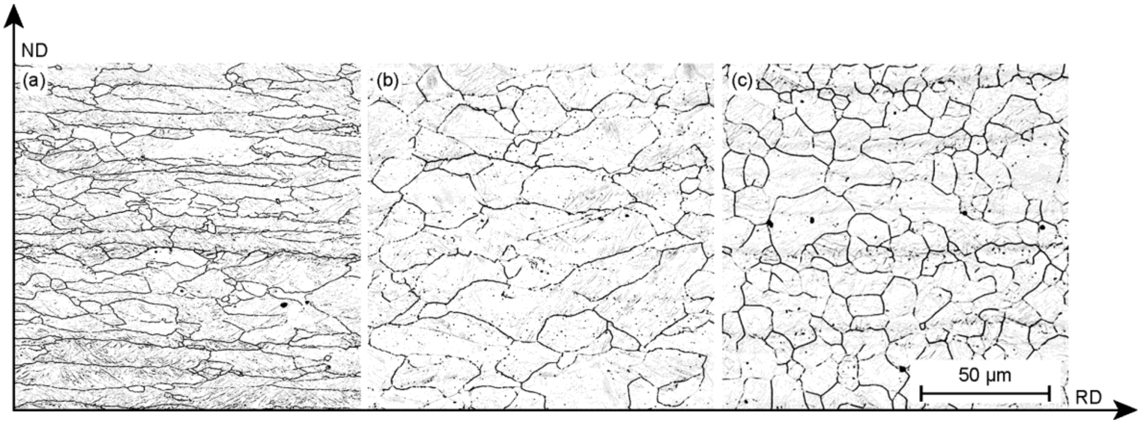

FIGURE 1. PAG morphology of (a) DQ_1, (b) DQ_2 and (c) RQ steels. ND = normal direction and TD = transverse direction.

TABLE 2. Mean PAG size (d_G), grain boundary surface area per unit volume (S_V), and RD/ND grain size ratio of each steel grade.

Steel grade	d_G (µm)	S_v (mm^2/mm^3)	RD/ND
DQ_1	10	272	3.0 ≈ 3
DQ_2	15	151	1.6 ≈ 2
RQ	10	208	1.1 ≈ 1

2.2 Test specimens

The novel tuning-fork specimens (Figure 2a) are utilized in this study [20,21]. The specimens were wire electrical discharge machined (WEDM) from 5 mm thick machined sheets and oriented so that the expected crack growth plane is either in the longitudinal or transverse direction in terms of rolling direction. The specimen orientations are labeled with a two-letter code (Figure 2b), where the first letter designates the direction normal to the crack plane and the second letter refers to the expected direction of crack propagation [25]. Prior to testing, the tensile stress surface area was mechanically polished using up to 240 grit discs to eliminate any possible microstructural changes caused by WEDM.

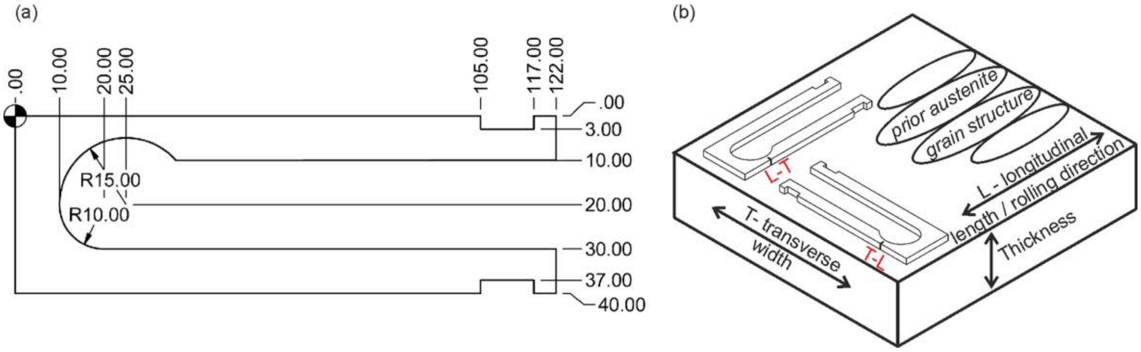

FIGURE 2. (a) Tuning-fork specimen with dimensions in mm, specimen thickness 5 mm. (b) Specimen and crack plane orientation codes.

Stressing of the tuning-fork specimens was conducted with a loadcell clamp, which pushes the specimen arms together while simultaneously measuring the applied force. Compressing the specimen arms towards each other creates an isolated tensile stress concentration on the outer part of the narrower arm, making it the single possible fracture area during the test (Figure 3). At the same time, an isolated compressive stress concentration is created on the inside part of the narrower arm. The distribution of the compressive stress is not relevant in the crack initiation and therefore it is not displayed in Figure 3. Stress distribution in the tuning-fork specimens during compression was analyzed with FEM software Abaqus [21] for each steel grade. Compressed specimen arm distance applied during the tests was calculated using this data.

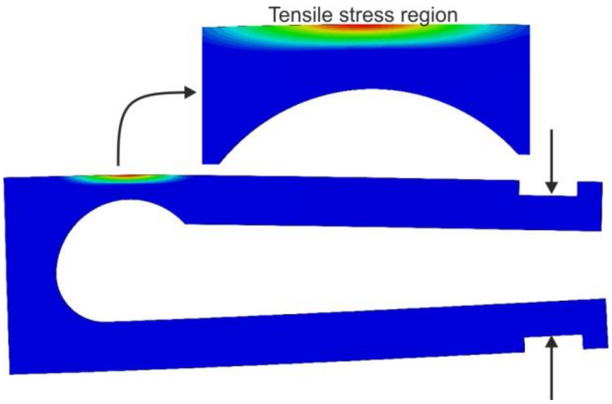

FIGURE 3. Stressed tuning-fork specimen with a tensile stress concentration on the outer part of the narrower arm.

2.3 Loadcell clamp

A new loadcell clamp was developed in this study for measuring the crack initiation time (t_i), propagation time (t_p), and time-to-fracture (t_f). The clamp has an integrated loadcell system, which monitors the clamp relaxation caused by crack initiation and propagation during the hydrogen charging experiments.

The loadcell was placed in a metal case where it can be moved forward with a screw. The loadcell and the screw are separated with a thin cylindrical piece of metal to protect the loadcell surface. At the opposite side of the loadcell, a metal rod (Ø4 mm) with a rectangular pressing piece is in contact with the specimen arm. The rectangular piece is used to even out the stress distribution on the specimen surface. When the screw is tightened, the loadcell moves forward pressing the metal rod, which subsequently pushes the specimen arms towards each other. Figure 4b presents the loadcell clamping arrangement with markings for all the moving parts.

2.4 Electrochemical hydrogen charging

Constant displacement tests were performed at room temperature with the potentiostatic hydrogen charging technique with a Gill AC Bi-STAT potentiostat using a -1200 mV potential and 0.1 M H_2SO_4 + CH_4N_2S (1 g/l) electrolyte. During hydrogen charging, a platinum-coated titanium plate was used as the counter electrode and Hg/Hg_2SO_4 electrode as the reference electrode, which was placed in the Luggin capillary. A special corrosion cell was built for the hydrogen charging experiments to fit the tuning-fork specimen and loadcell clamping system (Figure 4a). The corrosion cell comprises of a glass beaker and a removable plastic cap with holes for the electrodes.

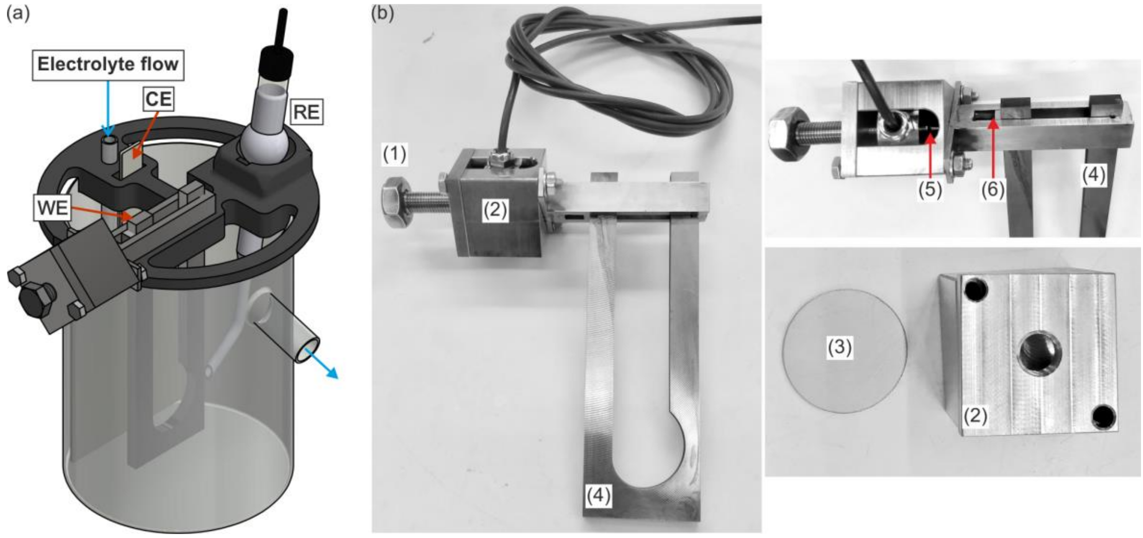

FIGURE 4. (a) 3D model of the corrosion cell utilized in hydrogen charging procedures, (b) Loadcell clamping system with (1) screw, (2) loadcell case, (3) cylinder part, (4) specimen, (5) metal rod and (6) rectangular pressing piece

In the beginning of each test, the electrolyte is de-aerated with nitrogen and stirred in a separate reservoir. Mixed and de-aerated electrolyte is pumped from the reservoir into the corrosion cell. During testing, more electrolyte is directed to the bottom of the cell with a rate of 2 ml/min, which was found to be optimal for maintaining a clear visibility. With lower speeds, the electrolyte gradually changed from clear to foggy, which affected the monitoring of the fracture appearance during testing. Excess electrolyte flows over through an outlet located at the top of the cell after reaching a certain critical level. This electrolyte circulation system enabled maintaining the same electrolyte level throughout all the tests. 3D model of the corrosion cell with the electrode and electrolyte flow markings is presented in Figure 4a.

2.5 Constant displacement tests

Tuning-fork tests with the loadcell clamping system were conducted at three different elastic stress levels: 1/3 R_m, 1/2 R_m, and 2/3 R_m, where R_m stands for the tensile strength of the material. For each test material and specimen type, 5 – 8 tests were conducted at stress levels 1/2 – 2/3 R_m, and 3 – 5 tests at stress level 1/3 R_m. The stressed tuning-fork specimens were charged with hydrogen up to t_f. The elastic tensile stress conditions change as a function of crack growth, and the obtained time-force data was used for the analysis of the HE process. Fracture surfaces were investigated with a Zeiss Sigma field-emission scanning electron microscope to understand differences in the hydrogen-induced cracking mechanism.

3 EXPERIMENTAL METHODS

To analyze the acquired time-force data systematically, effectively, and eliminating possible user errors, an automated data handling method and new software are developed in this study. The software has a graphical user interface (GUI), and it is coded with Python 2.7 programming language. The new software handles the time-force data filtering and finds the key parameters relevant for analyzing the test data. The details regarding the data analysis tool are explained in the following chapters.

3.1 Force data filtering

Unfiltered force data (1/s) was found to have a lot of random fluctuations that interfere with data analysis. To eliminate these fluctuations, different moving point averages were tested according to Equation 1,

$$F_{pi} = \frac{\sum_{i-p}^{i+p} F_i}{2p+1} \quad (1)$$

where F_{pi} = filtered force, p = filtering parameter, and F_i = raw force. Moving point averaging was chosen due to its simplicity and because it does not alter the observed signal form when dealing with data sets with a high amount of data points. 15 point moving average (2p + 1) was selected for data filtering, since increasing the averaging length did not have a meaningful effect after that point. Tested averaging options are presented in Figure 5.

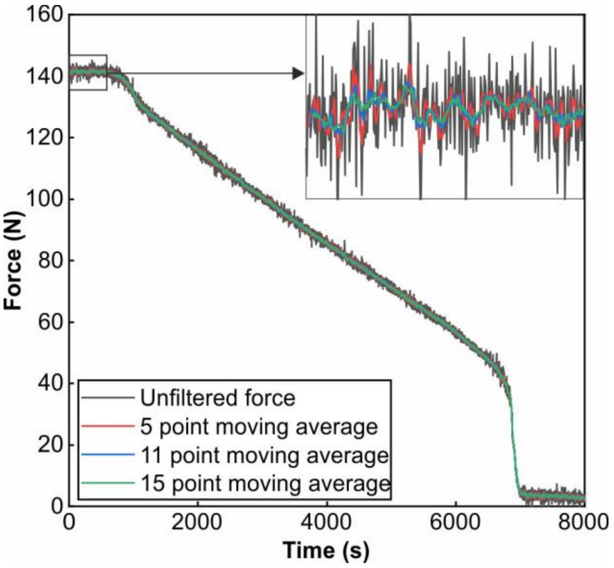

FIGURE 5. An example of force data with different filtering options as moving point averages.

3.2 Graph types

Depending on the test material and the applied stress level, 3 different graph types were identified. Graph type 1 was observed within the range 1/3 – 2/3 R_m of applied stress, and it shows three distinguishable parts: crack initiation, propagation, and final fracture (Figure 6). The crack initiation is visible in the beginning of the test as a plateau in the t-F data, which shows fluctuating force values in a fixed range. After a certain time period, the force values start to decrease gradually, which indicates that crack initiation and propagation have started. The force continues to decrease gradually until reaching a sudden drop, which designates the final fracture of the specimen. Without hydrogen charging, a constant initial force level is maintained. Three points are determined from the graph type 1: initiation time/propagation start (t_i), propagation finish (t_{pf}), and time-to-fracture (t_f). Propagation time ($t_p = t_{pf} – t_i$) and drop time ($t_d = t_f - t_{pf}$) are also determined from the plot. Figure 6 presents an example of real test data and schematics of graph type 1 with markings of defined point locations.

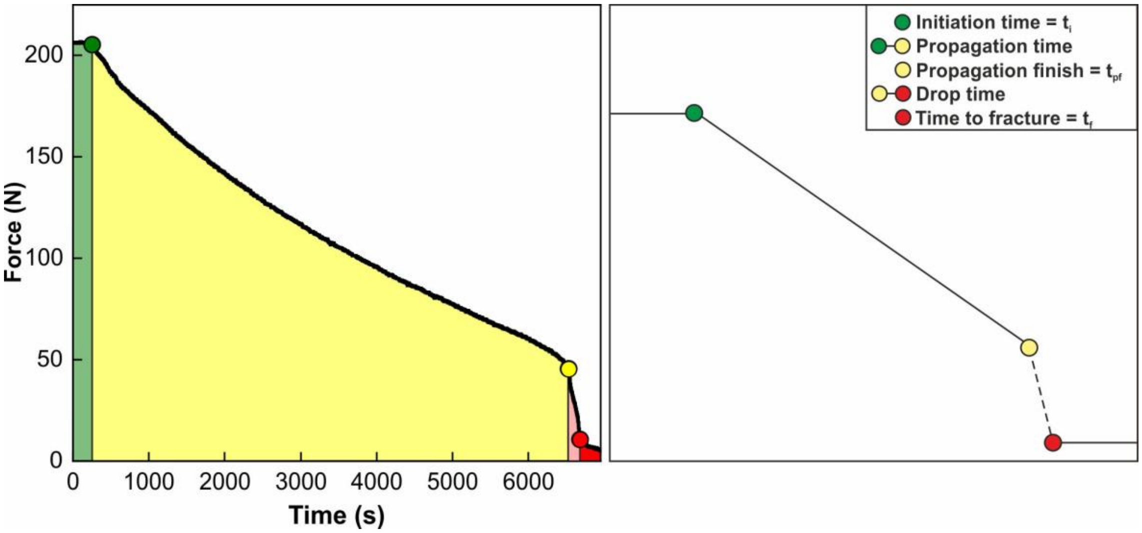

FIGURE 6. Graph type 1 with three points: initiation time (t_i), propagation finish (t_{pf}) and time-to-fracture (t_f). Green color presents initiation, yellow propagation, and shades of red the final fracture phases.

Graph type 2 was also observed within the range 1/3 – 2/3 R_m of applied stress, but unlike graph type 1 it has only two distinguishable parts: crack initiation and propagation (Figure 7). The crack initiation plateau is the same as in the graph type 1, but the crack propagation part is different since it does not lead to a sudden drop but continues steadily until the complete clamp relaxation with force values close to zero. Two points are determined from the graph type 2: crack initiation time/propagation start (t_i) and time-to-fracture (t_f). Based on these points, the crack propagation time ($t_p = t_{pf} – t_i$) is determined. Figure 7 presents an example of real data and the schematics of graph type 2 with the defined points. In both cases of graph type 1 and graph type 2, the crack propagation is not always completely linear but can have minor variations during the crack growth.

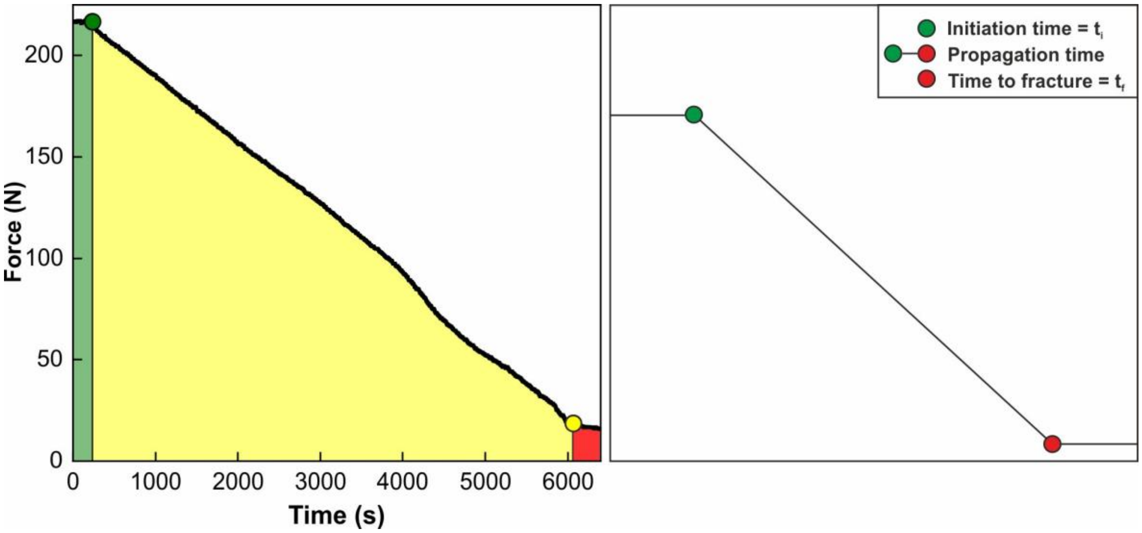

FIGURE 7. Graph type 2 with two points: crack initiation time (t_i) and time-to-fracture (t_f). Green color presents crack initiation, yellow propagation, and red final fracture phase.

Graph type 3 was only observed at stress level 1/3 R_m. It differs significantly from the graph types 1 and 2, since the crack initiation plateau phase continues throughout the test until the sudden drop in the force values (Figure 8). The force drop occurs straight from the initiation phase, which is considerably longer as compared to that in the graph type 1, where the sudden drop occurs after a marked decrease in the force values. From graph type 3, the same points are determined as in graph type 2: crack initiation time/propagation start (t_i) and time-to-fracture (t_f), which lead to the calculation of the drop time (t_d). Figure 8 illustrates an example and the schematics of point definition of graph type 3.

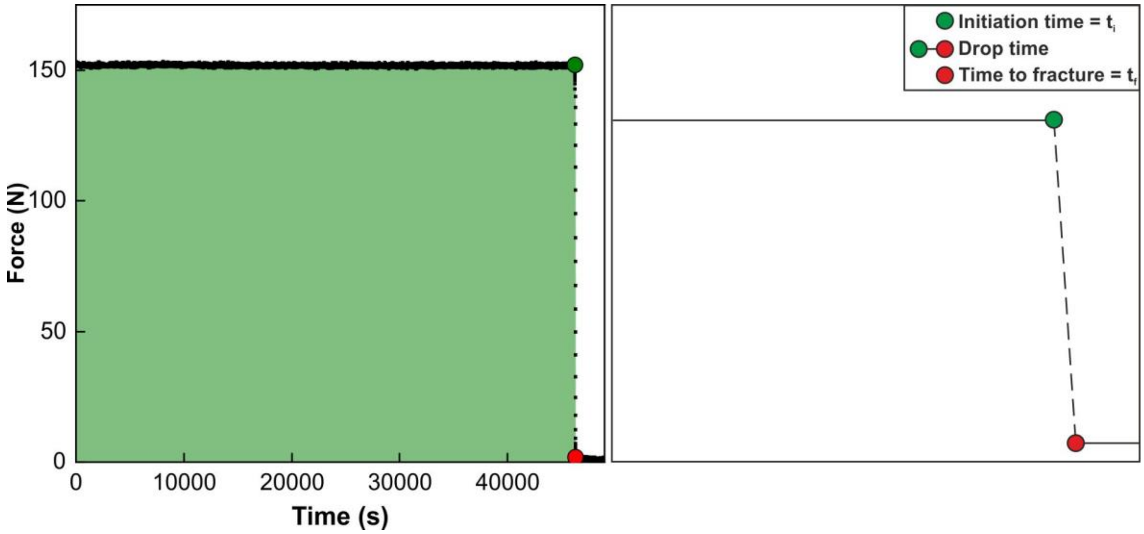

FIGURE 8. Graph type 3 with two points: crack initiation time (t_i) and time-to-fracture (t_f) with green color presenting the initiation phase.

3.3 *Data analysis methods*

Data analysis was conducted with the developed software, which automatically calculates times t_i, t_{pf}, and t_f with different techniques. The force graphs of the same material, specimen orientation, and stress level are handled simultaneously with the GUI tool. Each group produces average t_i, t_{pf}, t_f, and standard deviation (SD) values. For parameters used in the determination of the points, all data from 1/2 R_m and 2/3 R_m tests were analyzed.

3.3.1 *Initiation time*

Graph types 1 and 2 show a relatively short initiation time. Therefore, the x-axis (time) was converted to a log10 scale for better visualization. A horizontal start line was created at the first force data value to study the changing angle between the force data points and the start line as presented in Figure 9. This changing angle was named the start angle since it was used to calculate the crack initiation time according to Equation 2. The investigated point gap ($x_i \rightarrow x_{i+a}$) for the angle determination was 15 points.

$$\alpha_i \sphericalangle(l_1, l_2) = arctan(\frac{k_{i2}-k_{i1}}{1+k_{i1}k_{i2}}) = arctan(k_{i2}) \quad (2)$$

where $k = \frac{y_2-y_1}{x_2-x_1}, k_{i1} = 0 \ and \ k_{i2} = \frac{y_{i+a}-y_0}{x_{i+a}-x_i}, a = 15.$

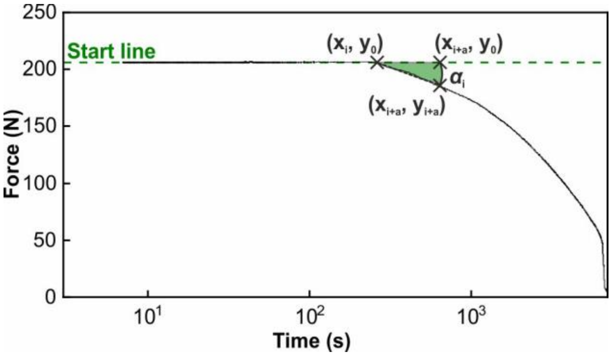

FIGURE 9. Angle calculation between the start line and the time-force data values.

The obtained start angle data is used to detect a significant change in the force values. Crack initiation and the beginning of the crack propagation phase can thus be established by considering the start angle values and selection of the specific limiting angle (α_{lim}). Using the limiting angle, t_i is determined according to Equation 3. The SD values for t_i with different limiting angle options are presented in Figure 10.

$$\text{If } (\alpha_i < \alpha_{lim}) \rightarrow t_{lim} = x_i \quad (3)$$

Considering the variation of the data in Figure 10, -5° was selected as α_{lim} for all the tests, as the variation started to increase with angles lower than -5°. With higher angle values, the variation increased for some of the steel grades. Figure 11 presents t_i determination from the t-F curve with α_{lim} = -5°.

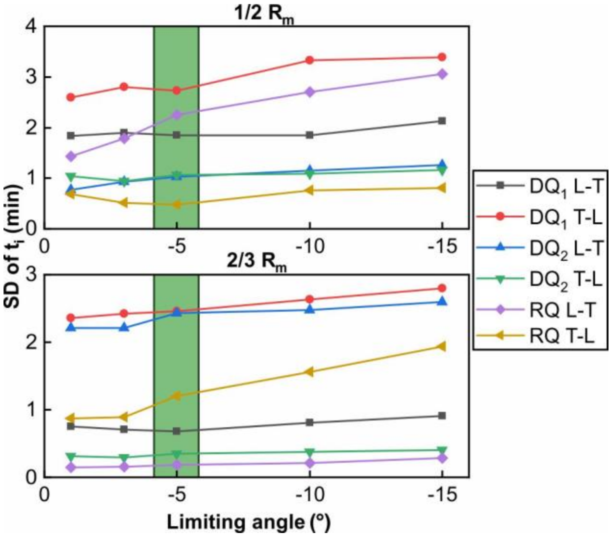

FIGURE 10. SD of crack initiation time (t_i) with changing limiting angle value.

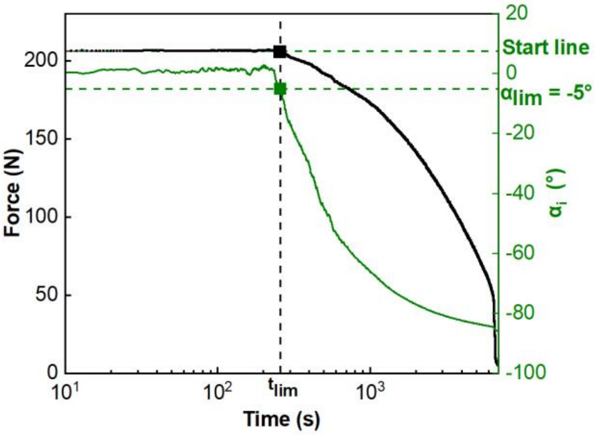

FIGURE 11. Force and start angle curves with marked points for limiting angle (α_{lim}) and crack initiation time ($t_{lim} = t_i$).

3.3.2 *Crack propagation finish*

Crack propagation finish point (t_{pf}) was calculated only for the type 1 graphs using the second derivative of the force data, which represents acceleration. The start of the final fracture, i.e. the sudden drop in t-F values, causes two significant peaks in the acceleration curve (Figure 12). The software calculates the start of the negative peak and then reduces the number of steps applied in the derivation procedures to counteract the offset. The obtained time value is $t_{pf.}$

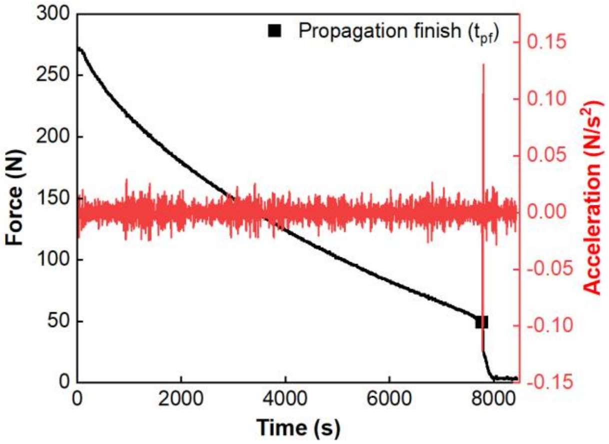

FIGURE 12. t-F data and its second derivative graph with marked crack propagation finish time (t_{pf}).

The first and second derivation can be executed with different step size options. The goal is to apply the smallest possible step size to maintain a good resolution with suppressed random noise in the signal. The SD of t_{pf} data was analyzed with different applied step sizes for type 1 graphs. Based on the variation, the smallest possible step size of 10 was selected for further data analysis (Figure 13). Variation remained approximately the same with bigger step size (15 – 50), but with lower values variation increased for some of the steel grades.

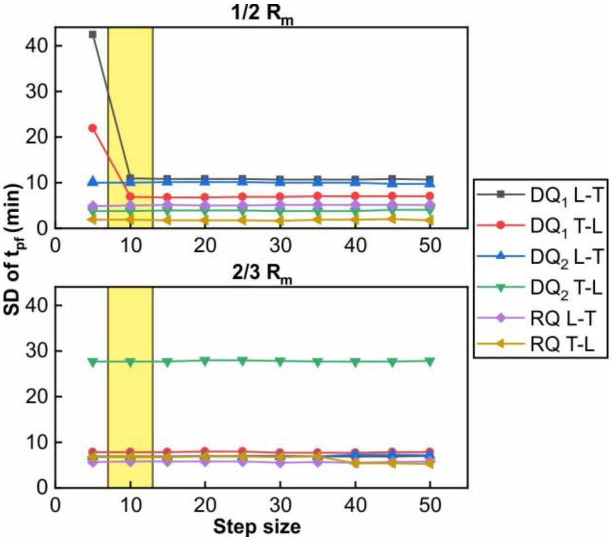

FIGURE 13. SD of crack propagation finish (t_{pf}) with changing step size values.

3.3.3 Time-to-fracture

Time-to-fracture (t_f) is determined with the same angle calculation procedure (see Equation 2) as used for t_i but in reverse, meaning that a reference line is drawn from the last force value of the overall t-F plot. For better visualization a linear time scale is used. The changing angle between the reference line and the force values was named as the end angle. Finally, the limit angle was selected from the end angle data for the determination of t_f. Standard deviations of t_f with different limiting angles are presented in Figure 14.

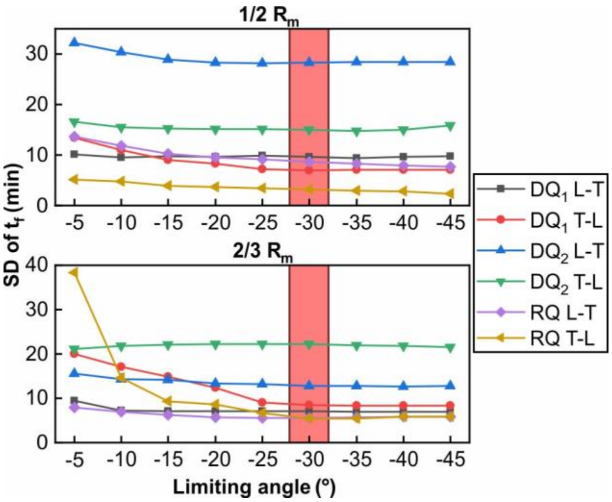

FIGURE 14. SD of time-to-fracture (t_f) with changing limiting angle values.

Based on the SD data, -30° was selected as α_{lim} for t_f determination. Higher end angles lead to increasing variation and with lower values the variation rose for some of the steel grades. Figure 15 demonstrates an example of the determination of t_f from the t-F curve with $\alpha_{lim} = -30°$. The selected limiting angle must be large enough because the test durations differ and some of the tests had a lot of excess data after fracture. If the applied α_{lim} was too small with a longer test time, the t_f observed by the tool may shift too far from the actual t_f due to the data. Limiting angle of -30° is applicable for both short and long time data.

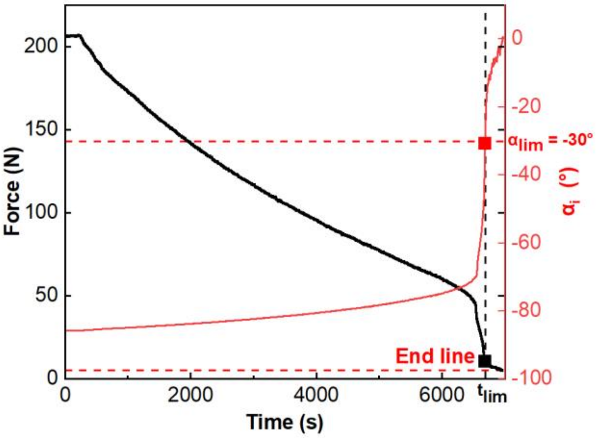

FIGURE 15. Force and end angle curves with marked points for limiting angle (α_{lim}) and time-to-fracture ($t_{lim} = t_f$).

3.4 *Defining of test results*

All obtained t-F graphs were divided into groups so that each group had the same material, specimen orientation, and applied stress level. For each group, average t_i, t_{pf}, t_f were calculated, and SD was determined for each point. All SD results at the same applied stress were combined and average SD was calculated for each time variable (Figure 16).

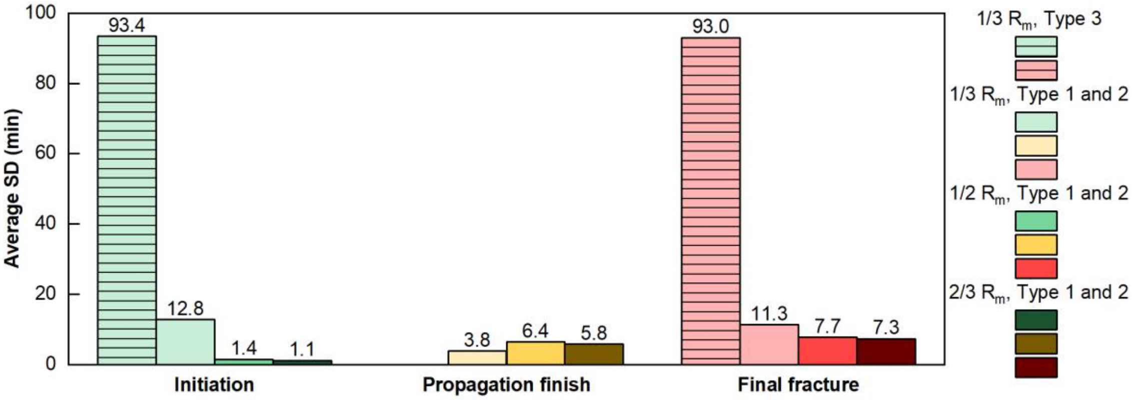

FIGURE 16. Average SD of all tested steel specimen types.

Average SD is the highest at the 1/3 R_m stress level, especially for the type 3 graphs. The exception is t_{pf}, where the stress level 1/3 R_m produced the lowest average SD. This is most likely due to a smaller number of tests because the majority of the tests at 1/3 R_m stress level produced type 3 graphs without the crack propagation phase. Hydrogen charging tests with graph type 3 exhibit also 2 – 4 times longer t_f when compared to the other graph types. With prolonged charging time, more hydrogen diffused to the region of tensile stress concentration until a certain critical hydrogen content was reached. Therefore, the higher hydrogen content most likely contributed to the fast fracture of the specimens in tests exhibiting type 3 graphs. Also, at lower stress levels, the effects of minor surface irregularities and near-surface inclusions are emphasized.

Stress levels 1/2 R_m and 2/3 R_m with type 1 and 2 graphs showed only minor differences in the average SD of t_i, t_{pf}, and t_f with less than a minute of a difference between each other. Therefore, both stress levels were selected for further analysis, while the 1/3 R_m stress level was excluded.

With the selected stress levels 1/2 R_m and 2/3 R_m, DQ_2 demonstrated partially anomalous results. Approximately 17% of all the conducted tests failed prematurely (fast tests) in comparison to the rest with notably longer t_f (normal tests). Fracture surfaces of both test types demonstrated distinct differences as presented in Figure 17. The samples, which took a long time to fail had a relatively smooth fracture surface in comparison to the fast tests with irregular and rough fracture surfaces.

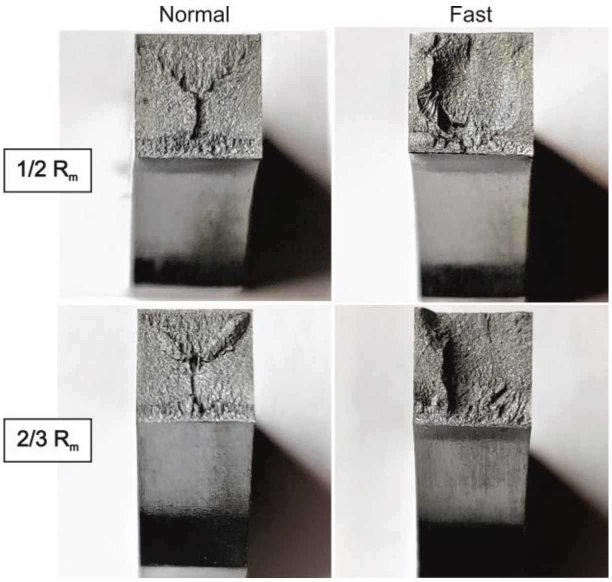

FIGURE 17. Fracture surfaces of normal and fast tests of DQ_2 steel conducted at stress levels 1/2 R_m and 2/3 R_m.

A possible explanation for this phenomenon is the higher S and Mn contents of DQ_2 (Table 1). Mn tends to segregate along the centerline and form MnS inclusions, which affect negatively hydrogen-induced cracking [2,3,5,26,27]. Therefore, lower Mn content of DQ_1 and RQ steels reduces the centerline segregation and the amount of MnS inclusions. The other investigated steel grades did not manifest a similar behavior, and therefore the shorter test results of DQ_2 were excluded from the final steel evaluation. Figure 18 presents the observed differences in t_f of DQ_2.

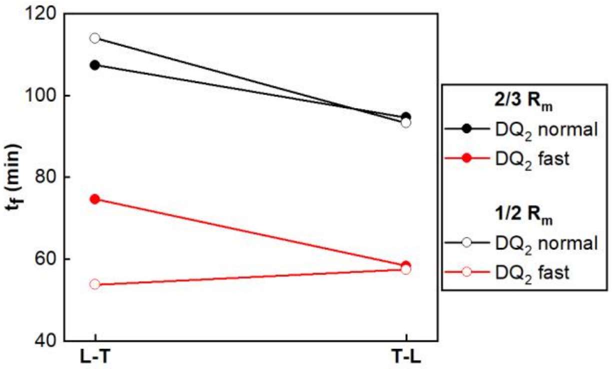

FIGURE 18. Comparison of average t_f of normal and fast tests of the DQ_2.

4 EXPERIMENTAL RESULTS AND DISCUSSION

4.1 *Microstructural anisotropy*

Ranking of the steels is conducted based on t_f results since it measures the overall susceptibility of the material in displacement-controlled testing. For each steel grade, the effect of microstructural anisotropy was investigated. In Figure 19, the effect of the microstructural anisotropy is demonstrated by comparing the L-T and T-L results (see Figure 2b) of all tested steel grades.

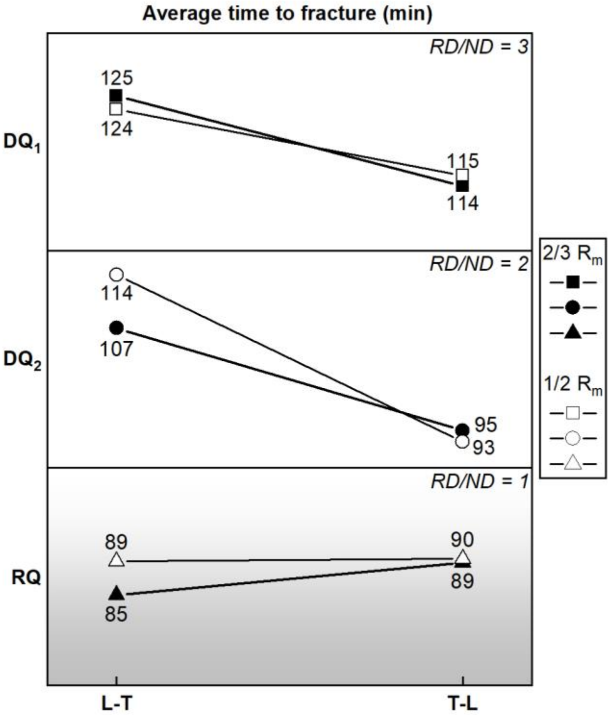

FIGURE 19. Average time-to-fracture at stress level 1/2 R_m and 2/3 R_m for the steel grades divided into L-T and T-L orientations.

For both DQ steels, microstructural anisotropy is evident with lower t_f values for the T-L specimens. DQ_2 has the biggest differences in t_f between the two specimen orientations, despite having less elongated PAGs than DQ_1. At the same time, RQ with an equiaxed PAG morphology shows only minor differences (1 – 4 min) between specimens of different orientations. Statistical difference between L-T and T-L specimens is calculated with T-test, and the results are given in Table 3. The t-test calculates probability error (p), and the differences between the two orientations are considered statistically significant when $p \leq 0.05$. Since no statistically significant anisotropy was observed for RQ, the t_f results of the different specimen orientations are combined.

TABLE 3. Probability error (p) of differently oriented specimens of each steel grade.

	DQ_1	**DQ_2**	**RQ**
1/2 R_m	0.047	0.001	0.471
2/3 R_m	0.023	0.001	0.156

The applied stress levels have a minor effect on the T-L specimens with 1 – 2 min t_f variations. The stress effect is more distinguished for the L-T specimens, which show 1 – 7 min variation in t_f. In both cases there is no systematic behavior in the stress level since in some cases t_f is longer at 2/3 R_m and in others at 1/2 R_m applied stress. However, the higher stress level produces a broader t_f range (107 – 125 min vs. 114 – 124 min) for the L-T specimens. With T-L specimens the width of the observed t_f range is almost the same (95 – 114 min vs. 93 – 115 min).

4.2 *Crack propagation phases*

Figure 20 presents the determined crack initiation, propagation, and final force drop regions and their proportions in the final time-to-fracture. The exact values of the obtained regions and t_f results are given in Table 4. The crack initiation times, and final force drop periods extend for all the tested steel grades at the lower stress level. The crack propagation phase shows the opposite behavior pattern, with t_p shortening at lower stress in all cases except for DQ_2 L-T. Therefore, the stress level of 1/2 R_m produced a more distinguishable crack propagation phase when compared to the 2/3 R_m stress level. The crack propagation phase represents a time-dependent subcritical crack growth caused by hydrogen. Therefore, the subcritical crack growth of different materials can be studied, and with a sufficient database used for life assessment of structural applications with hydrogen-induced cracks.

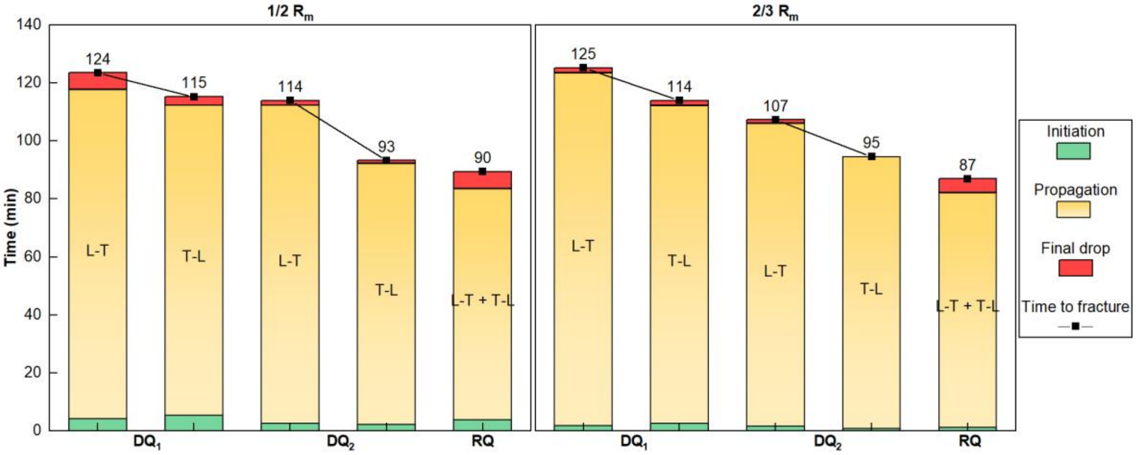

FIGURE 20. Time-to-fracture with proportions of crack initiation, propagation and final force drop regions of tests conducted at 1/2 R_m and 2/3 R_m stress levels.

TABLE 4. The numerical values of the investigated cracking phases in minutes.

Steel grade	**DQ_1 L-T**		**DQ_1 T-L**		**DQ_2 L-T**		**DQ_2 T-L**		**RQ**	
Stress of R_m	*1/2*	*2/3*	*1/2*	*2/3*	*1/2*	*2/3*	*1/2*	*2/3*	*1/2*	*2/3*
Initiation	4.3	1.8	5.5	2.6	2.6	1.7	2.3	0.8	3.9	1.2
Propagation	113.6	121.7	106.9	109.7	109.7	104.4	89.9	93.9	79.7	81.1
Drop	5.7	1.8	3.0	1.7	1.6	1.2	1.0	0.0	5.9	4.7
t_f	123.5	125.2	115.3	114.0	114.0	107.4	93.3	94.6	89.5	87.0

Both stress levels are used in the steel ranking since t_f results show the same order regardless of the stress level. Time-to-fracture is the longest for DQ_1, then DQ_2, and the shortest for RQ. However, the T-L specimens of DQ_2 show only small differences in t_f when compared to RQ. The obtained results indicate that the direction of the crack propagation in DQ steels affects t_f, and T-L specimens with crack propagation in the ND-RD direction fail faster in comparison to L-T specimens. Therefore, it is important to consider the direction of possible hydrogen-induced cracks in the structural design of applications, which are used in hydrogen-containing environments.

4.3 Fractography

The number of cracks formed in the hydrogen charging procedure depends on the applied stress level. Highest applied stress level 2/3 R_m produced the highest number of cracks and the widest region where the cracks are visible, i.e. the crack zone. At lower applied stress levels, the number of cracks decreases, and the crack zone is narrower. The lowest 1/3 R_m stress level produced in most cases only the final fracture. Figure 21 presents the dependence of the applied stress level on the shape of the stress concentration region and the number of cracks.

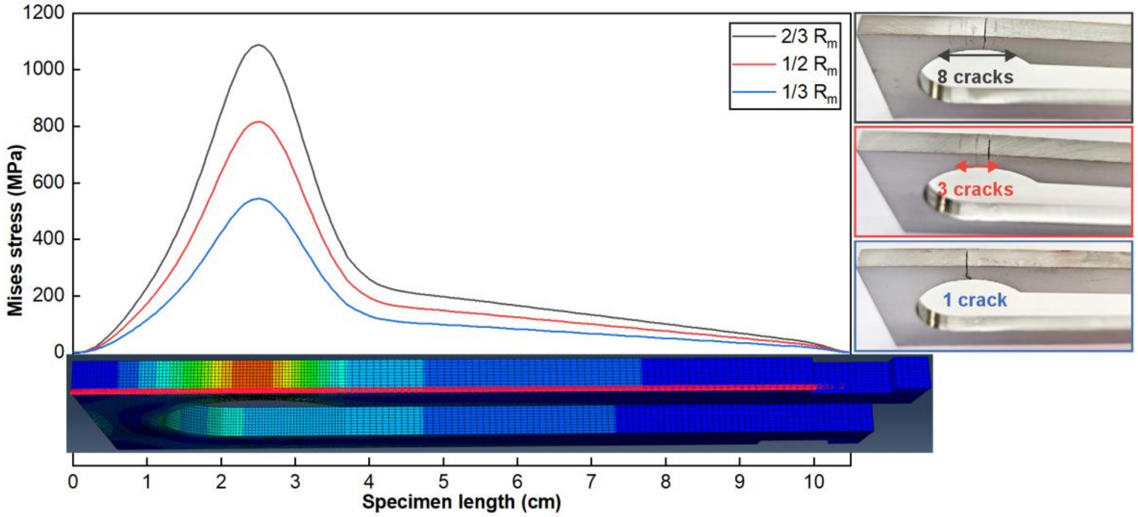

FIGURE 21. An example of stress distribution on the specimen surface during clamping.

The failure of the specimen is caused by the formation of one or by multiple cracks, which are initiated from the opposite corners of the specimen and join during the propagation phase. The two types of final cracks of DQ_1 steel are presented in Figure 22. The sudden drop in the t-F curves is likely due to the coalescence of the two opposite cracks.

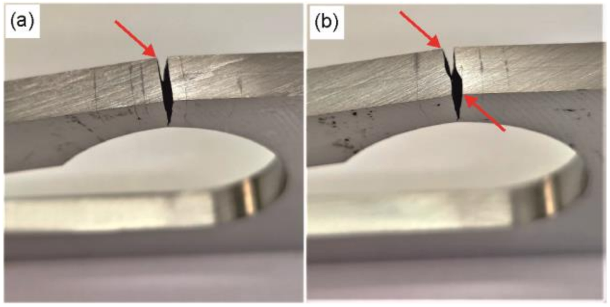

FIGURE 22. (a) One crack leading to final fracture, and (b) two joined cracks leading to a final fracture marked with red arrows.

Macroscopic fracture surface examination shows that the most corroded areas were at the top and the sides of the fracture surfaces. The corrosion product pattern indicates that the most corroded areas were exposed to the electrolyte longer, differentiating primary crack initiation and propagation phases. The corrosion products, fractography, and the FEM model indicate that the crack initiation starts from the edges/corners and the crack propagates towards the middle of the specimen leading to final fracture (Figure 23). The machined surfaces on the specimen sides have residual stress, which may also contribute to the crack initiation and propagation.

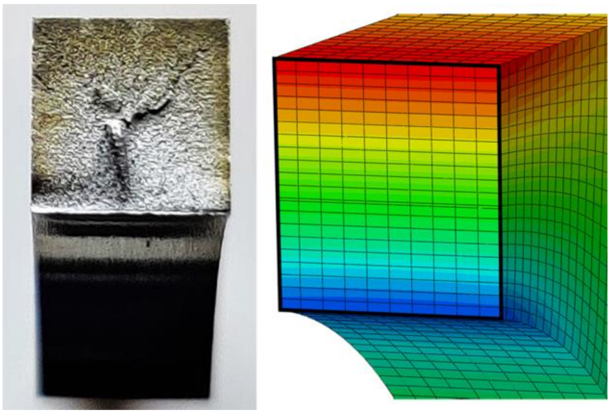

FIGURE 23. A fracture surface after hydrogen charging and the stress distribution across the expected crack plane. Red color represents tensile and blue compressive stress.

Fractographic analysis demonstrates significant differences between the fracture surfaces of DQ and RQ steels in Figure 24. For the DQ steels, the crack propagation is dominated by transgranular quasi-cleavage in both L-T and T-L specimens. RQ steel exhibits a pronounced intergranular crack propagation in both specimen orientations. Figure 24f shows, however, that the fracture surface morphology of the RQ steel exhibits the martensitic microstructural morphology instead of planar grain boundary surfaces. Therefore, the crack growth may have occurred also in the close vicinity of the grain boundaries.

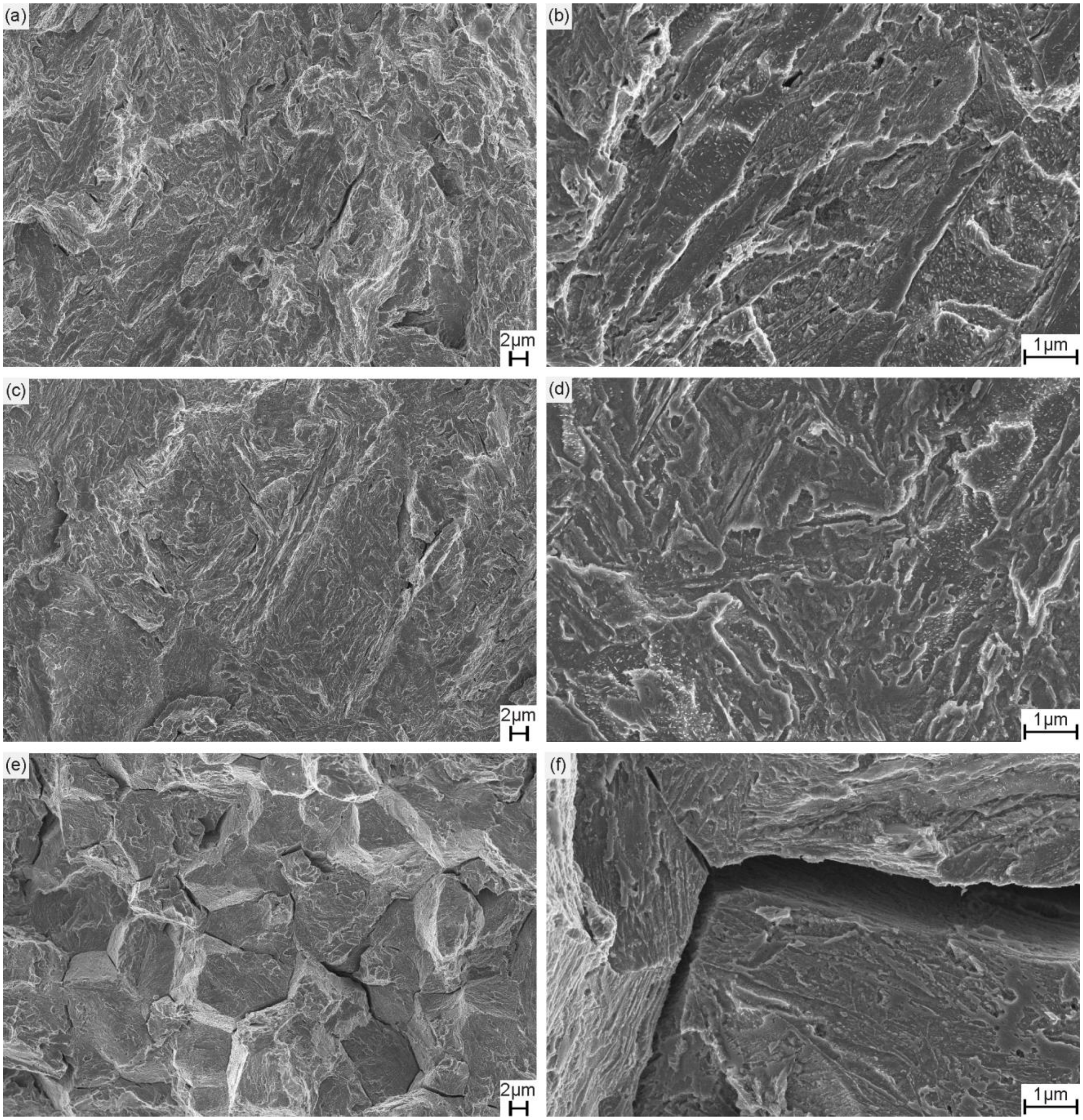

FIGURE 24. General and detailed views of fracture surfaces of investigated steel grades: (a and b) DQ_1, (c and d) DQ_2, and (e and f) RQ.

Differences in t_f between the two DQ steels are most likely due to the different alloy compositions and the grain boundary surface area per unit values (S_v). For L-T specimens, crack propagation occurs in the ND-TD plane, and for T-L in the ND-RD plane. For example, the average grain size of DQ_1 in TD direction is 11 µm and in RD direction 16 µm. A higher amount of grain boundaries on the crack path can slow down the crack propagation, which explains the differences in t_f results for L-T and T-L specimens.

However, the significantly shorter t_f of RQ can be taken as an indication that intergranular crack propagation is more detrimental than a transgranular quasi-cleavage. One of the main differences between the DQ and RQ steels is the PAG morphology. PAG size and shape are very important in terms of delayed fracture since elongated PAG structure has been reported to suppress intergranular fracture and improve HE resistance [8,28]. However, the chemical compositions of the studied DQ and RQ steels are different, thus, the significance of the PAG structure cannot be unambiguously quantified.

Estimation of the crack growth rate is possible with the obtained results by dividing the crack propagation time by the length of the fracture surface. However, only 1/3 R_m stress level tests produced a single crack, and even in those cases, the scatter was too substantial for a reliable evaluation. At higher stress levels, the crack growth rates would reflect the growth of the crack front rather than the growth of one final fracture. Therefore, the development of the test method has to be continued to enable the study of one final fracture with a suppressed scatter in crack growth rate. A potential solution for this is the use of notched tuning-fork specimens with a lower stress level.

5 CONCLUSIONS

This study presents the latest developments of the Tuning-Fork Test (TFT) [20,21] with modifications on the corrosion cell, the addition of the loadcell clamping system, and special software for the data analysis. The loadcell clamp together with the developed software allows monitoring of the crack initiation, propagation, and time-to-fracture of individual tests. Time-to-fracture (t_f) was selected as the steel ranking parameter in addition to the previously used threshold stress level. The utilization of time-to-fracture values significantly speeds up the testing procedure making the TFT a rapid and precise constant displacement test with good repeatability. The TFT method was used to test 500 HBW hard abrasion-resistant martensitic steels, two direct-quenched steels and one reheated and quenched steel, under potentiostatic hydrogen charging conditions at three elastic stress levels of 2/3 R_m, 1/2 R_m and 1/3 R_m. Tuning-fork specimens with parallel (L-T) or transverse (T-L) orientation in terms of the rolling direction were utilized in the hydrogen embrittlement experiments. Based on the scatter of the results, only stress levels of 1/2 R_m and 2/3 R_m were used in the steel ranking.

- The DQ steels with elongated PAG morphology showed shorter t_f for the T-L specimens, indicating their higher susceptibility to hydrogen embrittlement. With both specimen orientations, crack propagation was predominantly transgranular quasi-cleavage for the DQ steels.

- RQ with equiaxed PAG morphology did not exhibit significant differences between various specimens. With both specimen orientations, crack propagation was predominantly intergranular for RQ.

- Both applied stress levels produced similar t_f results with longest t_f for the low-Mn DQ_1 with most elongated PAG structure, followed by DQ_2 with higher Mn and S contents, and RQ.

- Different alloying, PAG structure, and crack path are the likely reasons behind the differing t_f, which indicates that direct-quenched steels with elongated PAG structure have superior resistance to hydrogen embrittlement in comparison to a reheated and quenched steel.

6 ACKNOWLEDGMENTS

This research was supported by Business Finland Oy. The authors wish to thank the technical staff of the Materials and Mechanical Engineering unit at the University of Oulu for their help with the experiments and sample preparation. The work of Kaarlo Vähätaini with the loadcell clamp is greatly appreciated. Dr. Pallaspuro thanks the Academy of Finland (#311934) for funding.

7 REFERENCES

1. J.S. Kim, H. Lee, D.L. Lee, K-T. Park, C.S. Lee, Materials Science and Engineering A 505, (2009): p. 105–110.
2. J. Kömi, P. Karjalainen, D. Porter, "Direct-Quenched Structural Steels," in *Encyclopedia of Iron, Steel, and Their Alloys* (Boca Raton, Florida: CRC Press, 2016), p. 1109–1125.
3. J. Venezuela, Q. Liu, M. Zhang, Q. Zhou, A. Atrens, Corrosion Reviews 34, 3 (2016): p. 153–186.
4. S. Ramamurthy, A. Atrens, Corrosion Reviews 31, 1 (2013): p. 1–31.
5. M.A. Al-Anezi, T.A. Al-Ghamdi, W.L. Al-Otaibi, S.M. Al-Muaili, "Manufacturing, Testing, and Operational Techniques to Prevent Sour Service Damages," in *Handbook of Materials Failure Analysis with Case Studies from the Oil and Gas Industry* (Oxford, United Kingdom: Elsevier, 2016), p. 393–410.
6. A. Kaijalainen, "Effect of microstructure on the mechanical properties and bendability of direct-quenched ultrahigh-strength steels" (PhD thesis, University of Oulu, 2016), p. 1–120.
7. A. Nagao, T. Ito, T. Obinata, JFE Technical Report 11, (2008): p. 13–18.
8. Y. Nie, Y. Kimura, T. Inoue, F. Yin, E. Akiyama, K. Tsuzaki, Metallurgical and Materials Transactions A 43A, 5 (2012): p. 1670–1678.
9. ASM International*, ASM Handbook, Volume 13C, Corrosion: Environments and Industries* (Materials Park, Ohio: ASM International, 2006), p. 1076.
10. G49-85, "Standard Practice for Preparation and Use of Direct Tension Stress-Corrosion Test Specimens" (ASTM, 2000), p. 1–6.
11. E1681-03, "Standard Test Method for Determining Threshold Stress Intensity Factor for Environment-Assisted Cracking of Metallic Materials" (ASTM, 2003), p. 1–13.
12. ASTM G38-01, "Standard Practice for Making and Using C-Ring Stress-Corrosion Test Specimens" (ASTM, 2001), p. 1–8.
13. SFS-EN ISO 7539-5, "Corrosion of Metals and Alloys. Stress Corrosion Testing. Part 5: Preparation and Use of C-Ring Specimens" (ISO, 1989), p. 1–21.
14. ASTM G30-97, "Standard Practice for Making and Using U-Bend Stress-Corrosion Test Specimens" (ASTM, 2016), p. 1–7.
15. SFS-EN ISO 7539-3, "Corrosion of Metals and Alloys. Stress Corrosion Testing. Part 3: Preparation and Use of U-Bend Specimens" (ISO, 1995), p. 1–13.
16. ASTM G129-00, "Standard Practice for Slow Strain Rate Testing to Evaluate the Susceptibility of Metallic Materials to Environmentally Assisted Cracking" (ASTM, 2000), p. 1–7.
17. A. Atrens, C.C. Brosnan, S. Ramamurthy, A. Oehlert, I.O. Smith, Measurement Science and Technology 4, 11 (1993): p. 1281–1292.
18. W. Dietzel, A. Atrens, A. Barnoush, "Mechanics of modern test methods and quantitative-accelerated testing for hydrogen embrittlement" in *Gaseous Hydrogen Embrittlement of Materials in Energy Technologies* (Woodhead Publishing, 2012), p. 237–273.
19. R. Baboian, *Corrosion Tests and Standards*, 2nd ed. (ASTM International, 2005), p. 373.
20. R. Latypova, T. Kauppi, S. Mehtonen, H. Hänninen, D. Porter, J. Kömi, Materials and Corrosion 70, 3 (2018): p. 521–528.
21. R. Latypova, T.T. Nyo, T. Kauppi, S. Pallaspuro, S. Mehtonen, H. Hänninen, J. Kömi, "Hydrogen-induced stress corrosion cracking studied by the novel tuning-fork test method," to be published at Materials and Corrosion (2020).
22. SFS-EN ISO 7539-1, "Corrosion of Metals and Alloys. Stress Corrosion Testing. Part 1: General Guidance on Testing Procedures" (ISO, 2012), p. 1–32.

23. O. Seppälä, S. Uusikallio, J. Larkiola, “A Tool for Computer-Aided Calculation of Grain Size,” XXVI International Conference on Computer Methods in Materials Technology KomPlasTech 2019, (AKNET-press, 2019), p. 128–130.
24. R.L. Higginson, C.M. Sellars, *Worked Examples in Quantitative Metallography* (Maney Publishing, 2003), p. 14.
25. ASTM E1823 − 13, “Standard Terminology Relating to Fatigue and Fracture Testing” (ASTM, 2013), p. 1–25.
26. T. Depover, A. Laureys, D.P. Escobar, E. Van den Eeckhout, E. Wallaert, K. Verbeken, Materials 11, 5 (2018): p. 1–25.
27. D. Hejazi, A.J. Haq, N. Yazdipour, D.P. Dunne, A. Calka, F. Barbaro, E. V. Pereloma, Materials Science and Engineering A 551, (2012): p. 40–49.
28. S. Yamasaki, T. Tarui, M. Kubota, Nippon Steel Technical Report 80 (1999): p. 50–55.